View Article Online / Journal Homepage / Table of Contents for this issue
Dynamic Article Links

Nanoscale

Cite this: *Nanoscale*, 2012, **4**, 7682

www.rsc.org/nanoscale

PAPER

PEG-capped, lanthanide doped GdF_3 nanoparticles: luminescent and T_2 contrast agents for optical and MRI multimodal imaging†

Tiziana Passuello,[a] Marco Pedroni,[a] Fabio Piccinelli,[a] Stefano Polizzi,[b] Pasquina Marzola,[c] Stefano Tambalo,[c] Giamaica Conti,[c] Donatella Benati,[d] Fiorenzo Vetrone,[e] Marco Bettinelli[a] and Adolfo Speghini*[a]

Received 10th July 2012, Accepted 17th October 2012
DOI: 10.1039/c2nr31796f

A facile method for the synthesis of water dispersible Er^{3+}/Yb^{3+} and Tm^{3+}/Yb^{3+} doped upconverting GdF_3 nanoparticles is reported. Strong upconversion emissions are observed in the red (for Er/Yb doped) and near-infrared (for Tm/Yb doped) regions upon laser excitation at 980 nm. The PEG coating ensures a good dispersion of the system in water and reduces the radiationless de-excitation of the excited states of the Er^{3+} and Tm^{3+} ions by water molecules. The r_2 relaxivity values are quite high with respect to the common T_2-relaxing agents ($22.6 \pm 3.4\ mM^{-1}\ s^{-1}$ and $15.8 \pm 3.4\ mM^{-1}\ s^{-1}$ for the Tm/Yb and Er/Yb doped samples, respectively), suggesting that the present NPs can be interesting as T_2 weighted contrast agents for proton MRI purpose. Preliminary experiments conducted *in vitro*, in stem cell cultures, and *in vivo*, after subcutaneous injection of the lanthanide-doped GdF_3 NPs, indicate scarce toxic effects. After an intravenous injection in mice, the GdF_3 NPs localize mainly in the liver. The present results indicate that the present Er^{3+}/Yb^{3+} and Tm^{3+}/Yb^{3+} doped GdF_3 NPs are suitable candidates to be efficiently used as bimodal probes for both *in vitro* and *in vivo* optical and magnetic resonance imaging.

1. Introduction

Lanthanide (Ln^{3+})-based inorganic nanoparticles (NPs) are an emerging class of advanced nanomaterials that can be successfully used in a variety of biomedical applications including optical imaging, contrast agents for magnetic resonance imaging (MRI), therapeutics, *etc.*[1–3] In particular, Ln^{3+}-doped NPs have been used as multiphoton imaging probes, which is the direct result of the exploitation of their upconversion (UC) properties. This process, inherent to the Ln^{3+} ions, allows for the (up) conversion of low energy excitation (typically near-infrared, NIR) to higher energies.[4–6] However, in contrast to most other two-photon excited materials (semiconductor quantum dots, gold nanorods, organic dyes, *etc.*), efficient UC emission in the UV-visible-NIR regions from Ln^{3+}-doped nanomaterials can be obtained using inexpensive diode NIR lasers (*e.g.* at 980 nm) as the excitation source. This is because "real" 4f electronic intermediate excited states, which possess long lifetimes and accordingly act as population reservoirs, partake in this multiphoton upconversion process. Thus, the process is a serial addition of NIR photons compared to the simultaneous absorption of photons in other materials, thereby eliminating the need for expensive and complex optical architecture.

In this context, water dispersible NIR-to-NIR upconverting NPs (UCNPs) can lead to prospective new advances in medical diagnostics and imaging.[7–9] This is mainly due to the weak fluorescence absorption of biological tissues in the 750–1000 nm region, ensuring a high degree of optical penetration not only for the excitation radiation but also for the emitted signal. Moreover, the NIR radiation can be easily detected by common CCDs (Charge Coupled Devices), already in place in optical imaging platforms thereby minimizing the need to upgrade to a new infrastructure. The optimal excitation/emission properties of these UCNPs have put them front and center in the development of multifunctional NPs. In combination with one (or more) other modality, these new NPs can allow for the delivery of multiple tools for imaging, diagnostics, and therapeutics (concomitantly or simultaneously) in one single platform.

In the context of disease detection, the advantages of having multiple imaging modalities are numerous. The coupling of optical multiphoton imaging with MRI would yield a nanoplatform with the ability to track the NPs with fast imaging times and optimal spatial resolution (through optical imaging) while

[a]*Dipartimento di Biotecnologie, Università di Verona and INSTM, UdR Verona, Strada Le Grazie 15, I-37134 Verona, Italy. E-mail: adolfo.speghini@univr.it*
[b]*Dipartimento di Chimica Molecolare e Nanosistemi, Università Ca' Foscari Venezia and INSTM, UdR Venezia, Via Torino 155/b, 30172, Venezia – Mestre, Italy*
[c]*Dipartimento di Informatica, Università di Verona and INSTM, UdR Verona, Strada Le Grazie 15, I-37134 Verona, Italy*
[d]*Dipartimento di Scienze Neurologiche, Neuropsicologiche, Morfologiche e Motorie, Università di Verona, I-37134 Verona, Italy*
[e]*Institut National de la Recherche Scientifique – Énergie, Matériaux et Télécommunications, Université du Québec, Varennes, QC J3X 1S2, Canada*

† Electronic supplementary information (ESI) available. See DOI: 10.1039/c2nr31796f

providing the three dimensionality and ability to get structural information associated with MRI.

Traditionally, gadolinium complexes have been used as contrast agents for MRI applications,[10–12] due to their paramagnetic properties resulting from the half filled 4f orbital (7 unpaired electrons) of the Gd^{3+} ions. Recent studies have also shown that GdF_3 and Gd_2O_3 NPs can induce a positive or negative enhancement of the contrast of MR images.[1–3,13–18] Given that these are nanocrystalline materials, they can be conveniently doped with minute amounts of luminescent Ln^{3+} ions rendering the exciting possibility of creating bimodal probes, capable of both multiphoton and magnetic resonance imaging. Previous studies have shown that Ln^{3+}-doped $NaGdF_4$ can be used as bimodal nanoprobes for both *in vitro* and *in vivo* MR and optical imaging.[4–6,19,20] Similarly, recent studies have also shown that GdF_3 NPs are efficient MR probes. In particular, water dispersible GdF_3 NPs doped with Eu^{3+}, Tb^{3+} and Dy^{3+} ions have been used as bimodal imaging probes where the dopant ions have emission in the visible region and can therefore be used as time-resolved photoluminescent (TRPL) probes.[7–9,21] Investigations on the UC emission of Ln^{3+}-doped GdF_3 NPs as powders[10–12,15,22,23] as well as on the synthesis and MRI properties of water dispersible undoped GdF_3 NPs[16,24] have been published. Very recently, Yin *et al.* analyzed the UC and MRI properties of Er/Yb/Li doped GdF_3 NPs calcined at 600 °C and successively coated them with a silica layer.[18] On the other hand, polyethylene glycol (PEG) is an interesting hydrophilic and also biocompatible capping agent commonly used for dispersing NPs in water solutions.[25–28] In particular, it is demonstrated that PEG coating is not toxic to cells in culture and, in some cases, stimulate cell aggregation and proliferation if PEG was added in culture medium.[29] In recent experiments the PEG-capped nanoparticle cellular uptake was investigated and in numerous experiments a higher uptake on PEG coated nanoparticles was demonstrated due to the higher affinity of tumor cells for this coating material.[30,31] For these reasons, we found it interesting to investigate the possibility of preparing PEG-capped, water dispersible GdF_3 based NPs, as bimodal probes for both optical and MRI contrast agents. In this work, we study the luminescence and contrast agent properties of PEG-capped Tm^{3+}/Yb^{3+} or Er^{3+}/Yb^{3+} GdF_3 NPs, prepared by a facile, environmentally friendly, one-pot hydrothermal synthesis, using water as a solvent. Two-photon excited UC and MRI *in vivo* properties are also investigated, as well as the NP cytotoxicity.

2. Experimental section

Appropriate amounts of the metal chlorides $GdCl_3$ (Aldrich 99.99%), $ErCl_3$, $TmCl_3$, and $YbCl_3$ (Aldrich 99.9%) were dissolved in 17 ml of deionized water, in order to obtain a total metal concentration equal to 0.124 M and Gd : Ln : Yb = 0.78 : 0.02 : 0.20 molar ratios (Ln = Er or Tm). To this metal solution, a stoichiometric amount of NH_4F (Aldrich, 99.9%) was dissolved with PEG 10 000 (Aldrich, 99.99%), in order to have a water : PEG mass ratio equal to 1. The resultant suspensions were heat-treated in a 100 ml stainless steel Teflon lined digestion pressure vessel (DAB-2, Berghof) at 200 °C for 8 h. After washing with acetone and drying at room temperature, the obtained NPs were directly dispersed in water. The dispersions remained stable for about one week. The same procedure was used to prepare uncapped Er^{3+}/Yb^{3+} or Tm^{3+}/Yb^{3+} doped GdF_3 NPs with the same lanthanide concentrations. For these NPs, PEG was not added as a starting reagent.

Mineralization of the NPs for ICP-MS analysis was carried out by weighing 15 mg of the NPs and adding 0.5 g of boric acid, 7 ml of hydrochloric acid (99.999%, Aldrich) and 1 ml of nitric acid (99.999%, Aldrich) in a Teflon container and heating in a microwave digestor (Start D, Milestone) for 10 min at 220 °C and then for 20 min at 220 °C. The obtained sample was properly diluted with deionized water and analyzed with an Agilent 7600 series ICP-MS instrument. The Gd^{3+} concentration in the water dispersions of the GdF_3 NPs was obtained using a calibration curve.

X-Ray powder diffraction (XRPD) patterns were measured with a powder diffractometer (Thermo, ARL XTRA), operating in Bragg–Brentano geometry, equipped with a Cu anode X-ray source ($K\alpha = 1.5418$) and using a Peltier Si(Li) cooled solid state detector. The spectra were collected with a scan rate of 0.04° s^{-1} in the 15°–90° 2θ range. The NP samples were finely ground in a mortar and then deposited in a low background sample stage for the measurements. The Rietveld refinements of the XRPD patterns were carried out using the MAUD software.[32]

Room temperature infrared absorption spectra were collected in the mid-infrared (MIR) region using a FTIR spectrometer (Nicolet, Magnet-IR 760) with a spectral resolution of 2 cm^{-1}. For the measurements, the NP samples were mixed with KBr (3 wt%) and pressed to obtain a pellet.

Transmission electron microscopy (TEM) and high resolution TEM (HRTEM) images of the NPs were obtained using a JEOL 3010 high resolution electron microscope (0.17 nm point-to-point), operating at 300 KV, equipped with a Gatan slow-scan CCD camera (model 794) and an Oxford Instrument EDS microanalysis detector (Model 6636). The NPs were dispersed in a toluene solution and deposited on a holey carbon film. A Philips Morgagni 268D transmission electron microscope operating at 80 kV equipped with a MegaView II camera was used for the tissue morphological analysis.

In order to obtain tissue images, three four-week old athymic mice (30 grams each) were used (obtained from Harlan Laboratories, Italy). The mice were anesthetized using 1% of isofluorane inhalation and a 200 μl dispersion of NPs (5 wt%) was administered subcutaneously thereafter. After 30 min the animals were sacrificed and a sample of epidermis was processed for histological evaluation by TEM to verify the internalization of NPs by epithelial cells or their distribution in the extracellular compartment. Samples were fixed in 2% glutaraldehyde for two hours and post-fixed in a water solution of osmium tetraoxide (1%) for a further two hours. After fixation, samples were treated with scalar concentrations of acetone and then fixed in Epon-Araldite. Ultra thin sections were obtained with a microtome and observed using electron microscopy.

UC luminescence spectra (with a spectral resolution of 0.1 nm) were collected upon continuous wave laser excitation at 980 nm using a diode laser (CNI Optoelectronics Tech). The emission signal was analyzed using a half-meter monochromator (HR460, Jobin Yvon) equipped with 1200 lines per mm grating and detected with a CCD detector (Spectrum One, Jobin Yvon). The comparison between the UC spectra of the uncapped and capped NPs has been carried out using the same equipment described above but using 150 lines per mm grating. In this case, the

spectral resolution of the spectra is of 0.8 nm. The upconversion luminescence photos under solar light illumination were acquired using a Canon CCD camera.

Two-photon upconversion images were acquired with a confocal Leica TCS SP5 System, using a Coherent Chameleon-Ultra Ti : sapphire pulsed laser as the excitation source in the near-infrared region (975 nm).

Longitudinal (r_1) and transversal (r_2) relaxivities were measured using imaging sequences according to Masotti *et al.*[33] Experiments were carried out at 22 °C using a Biospec Tomograph System (Bruker, Karlsruhe, Germany) equipped with a 4.7 T, 33 cm bore horizontal magnet (Oxford Ltd, UK) and with a gradient insert of 20 G cm^{-1} strength. A 72 mm internal diameter birdcage volume coil was used. Solutions of samples containing different concentrations of $GdF_3 : Er^{3+}/Yb^{3+}$ (from 0.05 to 1.67 mM) or $GdF_3 : Tm^{3+}/Yb^{3+}$ (from 0.04 to 1.30 mM) were prepared in water. The transversal relaxation times were measured using a standard Spin-Echo Multi-Echo sequence with the following parameters: TR/TE = 2000/15 ms, FOV = 120 × 60 mm^2, matrix size = 256 × 128, slice thickness = 2 mm, and number of echoes = 30. For the measurement of the longitudinal relaxation time, a fast T_1 mapping technique based on an IR-SNAPSHOT sequence was used.[15] The acquisition parameters were: FOV = 120 × 60 mm^2, matrix size = 128 × 128, slice thickness = 2 mm, TR/TE = 10/3.6 ms, and excitation pulse angle = 5°. The acquisition was segmented in 8 steps in order to obtain enough time resolution to monitor the recovery of the longitudinal magnetization. Longitudinal and transversal relaxation rates ($1/T_1$ and $1/T_2$) were plotted as a function of the gadolinium concentration and r_1 and r_2 relaxivities were obtained by the slope of the fitted straight line.

Mesenchymal stem cells were extracted from adipose tissue of mice (adipose-derived mesenchymal stem cells, ASCs) and were cultured in Dulbecco's Modified Eagle's Medium (DMEM) supplemented with 1% mixture of antibiotics and antimicotics and 20% fetal bovine serum (FBS) in 75 cm^2 plates. Cells were incubated at 37 °C and 5% of CO_2 for 24 h. When at confluence, the cells were treated with 1% trypsin and harvested. The cells were placed in 15 ml tubes and centrifuged for 5 min at 3000 rpm. The pellet at the bottom of the vials was suspended in 1 ml of growth medium and successively the amount of cells was determined by counting using a Burker chamber. Subsequently, the solution containing the cells was diluted and 100 000 cells were plated in a 96-well plate. For each well, 200 µl of fresh complete growth medium was added. Cells were incubated at 37 °C and 5% of CO_2 for 24 h.

When cells were at confluence, the culture medium was discarded and replaced with 200 µl of fresh growth medium containing the $GdF_3 : Er^{3+}/Yb^{3+}$ or $GdF_3 : Tm^{3+}/Yb^{3+}$ NPs. The concentration of GdF_3 used for this experiment was 2 mM. The GdF_3 NPs were compared with the clinical grade contrast agent Magnevist (Bayer Schering Pharma, Germany), at the same Gd concentration (2 mM). Cells were incubated at 37 °C and 5% of CO_2 for 6 h. After the incubation time the growth medium containing the NPs or Magnevist was removed and discarded. The cells were washed three times with sterile phosphate buffer (PBS) to remove the growth medium containing the NPs. Successively, 100 µl of fresh growth medium were placed in each well. The viability of cells was determined with the addition of 100 µl of 3-(4,4-dimethyl-2-triazolyl)-2,5-tetrazolium diphenyl bromide (MTT) in the growth medium, which was internalized by living cells and converted into insoluble formazan resulting from the cellular ATP production. The concentration of living cells was determined spectrophotometrically at 590 nm.

In order to obtain a preliminary evaluation of the potential usefulness of GdF_3 NPs as *in vivo* contrast agents, two Balb/c, male mice (6–8 weeks old) were intravenously injected with NPs at a dosage of 6 mg of Gd per kg. For MRI acquisitions, animals were anesthetized with gas anaesthesia (a mixture of O_2 and air containing 1–1.5% of isofluorane), placed in a heated animal bed and inserted in a 3.5 cm internal diameter bird-cage coil. T_2-weighted images of the mice body were acquired at 4.7 T using a Rapid Acquisition with Relaxation Enhancement (RARE) sequence with the following parameters: FOV = 5 × 5 cm^2, MTX = 256 × 256 pixels, slice thickness = 0.1 cm, TE_{eff} = 56 ms and TR = 5000 ms. The images were acquired before 20 and 40 min after GdF_3 NPs injection.

3. Results and discussion

Before any biological study could be carried out, it was necessary to undertake a thorough physico-chemical and morphological characterization of the Ln^{3+}-doped GdF_3 NPs. Since the crystalline phase of the inorganic NPs can yield valuable clues about their photophysical behavior, we initially undertook an XRPD study. Fig. 1a and SF1 (*cf.* ESI†) show the XRPD patterns with the Rietveld refinements using the MAUD software, for the PEG-capped Tm^{3+}/Yb^{3+} and Er^{3+}/Yb^{3+} co-doped GdF_3 NPs, respectively. In Fig. SF2 (*cf.* ESI†), the XRPD pattern for the uncapped $GdF_3 : Er^{3+},Yb^{3+}$ NPs is also shown. The peak positions and intensities of the XRPD patterns for PEG-capped and uncapped samples closely match those of the calculated pattern for orthorhombic GdF_3 (*Pnma* space group, PDF card no. 00-012-0788). In this crystal structure, the Gd^{3+} cations occupy a single site with an eight-fold F^- coordination (a ninth F^- ion is located at a much greater distance from Gd^{3+}) and C_s site symmetry. No additional peaks due to different phases were found, assuring that the samples were single phase. A Rietveld analysis, under the isotropic crystallite shape assumption, shows an average crystallite size of 71(1) nm and 80(1) nm for the

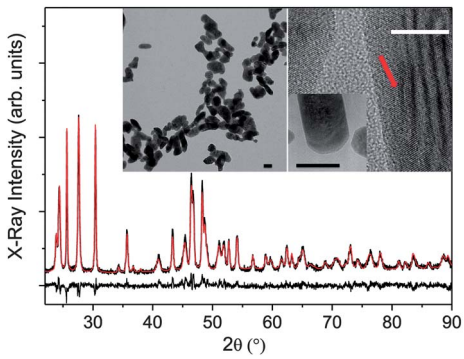

Fig. 1 XRPD pattern (black) and Rietveld refinement (red) for $GdF_3 : Tm^{3+}/Yb^{3+}$ NPs (Rw = 0.0795) prepared at 200 °C. Lower curve: residuals. Insets: TEM images of the GdF_3 NPs (the black and white scale bars indicate 100 and 10 nm, respectively). The HRTEM image shows (200) lattice planes (d = 3.2 Å), indicated by a red arrow.

Tm^{3+}/Yb^{3+} and Er^{3+}/Yb^{3+} co-doped GdF_3 NPs, respectively (see Fig. 1). Moreover, a Rietveld refinement of the XRPD patterns for the uncapped Tm^{3+}/Yb^{3+} and Er^{3+}/Yb^{3+} doped GdF_3 NPs shows an average particle size of 65(3) nm and 75(3) nm, respectively, similar to those found for the PEG-capped NPs. The successful substitution of the Ln^{3+} dopant ions into the Gd^{3+} site of the crystal structure dopants was demonstrated by the contraction of the unit cell volume of the doped samples with respect to the undoped one, due to the smaller ionic radius of Yb^{3+}, Er^{3+} and Tm^{3+} with respect to the Gd^{3+} ion (see Table 1). The synthesis of the PEG-capped NPs has been optimized by preparing different lanthanide doped GdF_3samples using the same experimental conditions except for the reaction temperature. In particular, we prepared samples at temperatures of 140 °C, 160 °C, 180 °C and 200 °C, maintaining the same reaction time, of 8 hours. We have included in the ESI† the XRPD patterns of such samples (Fig. SF3†). In all cases, pure phase orthorhombic GdF_3 NPs were obtained, with the average size slightly increasing with the heat treatment temperature. Moreover, in all the samples prepared with different heat treatment temperatures, no presence of the hexagonal GdF_3 phase was observed. After a thorough UC investigation using identical experimental setup and conditions, we determined that the NPs prepared at 200 °C showed the highest emission intensity and therefore these samples were used for all subsequent studies. Furthermore, the TEM images reveal an anisotropy of the particle shape (Fig. 1, insets) and both the Tm^{3+}/Yb^{3+} and Er^{3+}/Yb^{3+} doped PEG-capped GdF_3 NPs appear to be rod-shaped. The size distribution of the short edge size for the NPs and the aspect ratio are shown in the ESI (Fig. SF4 and SF5†). The average short edge size is around 85 nm, and the size dispersion is around 20 nm. The calculated average aspect ratio is around 1.8, with a dispersion of about 0.8.

To determine the success of the PEG capping, we performed FTIR spectroscopy where the mid-infrared spectrum of the GdF_3 NPs showed the typical features of the PEG molecule (Fig. 2). Bands due to stretching vibrations of the methylene group (around 2800 cm^{-1}) and strong bands attributed to the C–O and C–C stretching vibrations (in the range of 980–1200 cm^{-1}) were observed.[34] As evidenced in Fig. 2, the bands of the NPs coincide with those observed for the PEG polymer,[35] confirming the presence of PEG on the surface of the GdF_3 NPs. Moreover, the vibrational energy of the C–O–C stretching of the PEG polymer,[36,37]centered around 1110 cm^{-1}, is slightly but clearly decreased for the PEG-capped NPs with respect to the pure PEG polymer (see Fig. 2, inset). This behavior can be explained by a weak coordination bond of the oxygen lone pair with the metal ions (Gd^{3+}, Yb^{3+}, Er^{3+} or Tm^{3+}) at the NP surface. This weak interaction is most likely also responsible for the adhesion of the PEG polymer on the inorganic NPs.

Table 1 Unit cell parameters (*a*, *b*, *c* and volume) for Er^{3+}/Yb^{3+} and Tm^{3+}/Yb^{3+} codoped nanocrystalline GdF_3. The phase is orthorhombic (*Pnma* space group)

Sample	*a* (Å)	*b* (Å)	*c* (Å)	Unit cell volume (Å^3)
Undoped GdF_3[a]	6.571(1)	6.985(1)	4.393(1)	201.63(1)
$GdF_3 : Er^{3+},Yb^{3+}$	6.488(1)	6.943(1)	4.406(1)	198.47(1)
$GdF_3 : Tm^{3+},Yb^{3+}$	6.486(1)	6.944(1)	4.408(1)	198.53(1)

[a] Crystallographic data from PDF card no. 00-012-0788. Ionic sizes (in eight-fold coordination):[44] 1.20 Å for Gd^{3+}; 1.12 Å for Yb^{3+}; 1.14 Å for Er^{3+}; and 1.13 Å for Tm^{3+}.

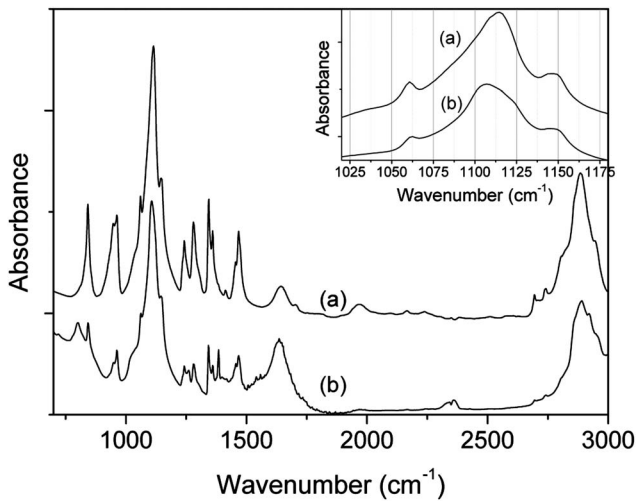

Fig. 2 FTIR spectra in the mid-infrared region (MIR) for PEG (a) and PEG-capped GdF_3 NPs (b).

Our ultimate goal is to use Ln^{3+}-doped NPs as a bimodal imaging platform (fluorescence and magnetic resonance imaging). Thus, we initially investigated the luminescence properties of $GdF_3 : Tm^{3+}/Yb^{3+}$ and $GdF_3 : Er^{3+}/Yb^{3+}$ NPs. In particular, we studied their UC properties, that is, their ability to emit light at higher energies compared to the excitation wavelength, *via* the multiphoton process known as UC. The UC spectra (λ_{exc} = 980 nm) of a water dispersion of Tm^{3+}/Yb^{3+} co-doped GdF_3 NPs show two very weak groups of bands in the 450–500 nm region, weak bands in the 650–700 nm region and a very strong band in the NIR region around 800 nm (Fig. 3a). These emission bands can be assigned to the Tm^{3+} transitions as follows: (i) $^1G_4 \rightarrow {}^3H_6$, $^1D_2 \rightarrow {}^3F_4$; (ii) $^1G_4 \rightarrow {}^3F_4$; (iii) $^3H_4 \rightarrow {}^3H_6$, $^1G_4 \rightarrow {}^3H_5$. A water dispersion of the Er^{3+}/Yb^{3+} co-doped GdF_3 NPs shows UC emission bands of the Er^{3+} ion in the green and red regions of the spectrum (Fig. 3b) and can be assigned to the following Er^{3+} transitions: (i) ($^2H_{11/2}$,$^4S_{3/2}$) $\rightarrow$ $^4I_{15/2}$; (ii) $^4F_{9/2} \rightarrow {}^4I_{15/2}$. From the UC spectrum it can be noted that the red emission is much stronger than the green one. The UC spectrum of the $GdF_3 : Er^{3+}/Yb^{3+}$ NPs in the dry powder form (shown in Fig. SF6†) shows strong red emission, behavior similar to that observed for Er^{3+}/Yb^{3+} co-doped nanocrystalline oxides with high Yb^{3+} concentration, *e.g.* for Y_2O_3 NPs.[38] It is worth noting that the red UC emission is maintained, in the water dispersion of the $GdF_3 : Er^{3+}/Yb^{3+}$ NPs. The details of the power study, which provides confirmation on the number of photons partaking in the upconversion process, are reported in the ESI, Fig. SF7, SF8 and SF9.† It should be noted that the UC emissions for water dispersible GdF_3 are easily measurable for excitation power densities as low as 40 W cm^{-2} (Fig. SF7, ESI†).

A comparison between the UC spectra of the uncapped and PEG-capped NPs was carried out, in order to ascertain the influence of the capping layer on the luminescence properties. The spectra were recorded for NP water dispersions with exactly

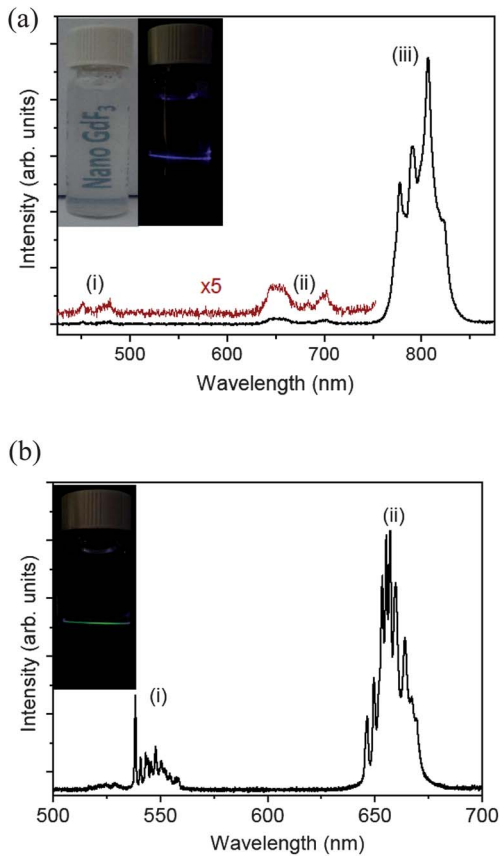

Fig. 3 UC spectra ($\lambda_{exc} = 980$ nm) of water dispersions of PEG-capped $GdF_3 : Tm^{3+}/Yb^{3+}$ (upper panel) and $GdF_3 : Er^{3+}/Yb^{3+}$ (lower panel) NPs (1.2 g l^{-1} concentration). Insets: pictures of PEG-capped GdF_3 water dispersions upon solar and 980 nm continuous wave diode laser illumination (laser power of 800 mW).

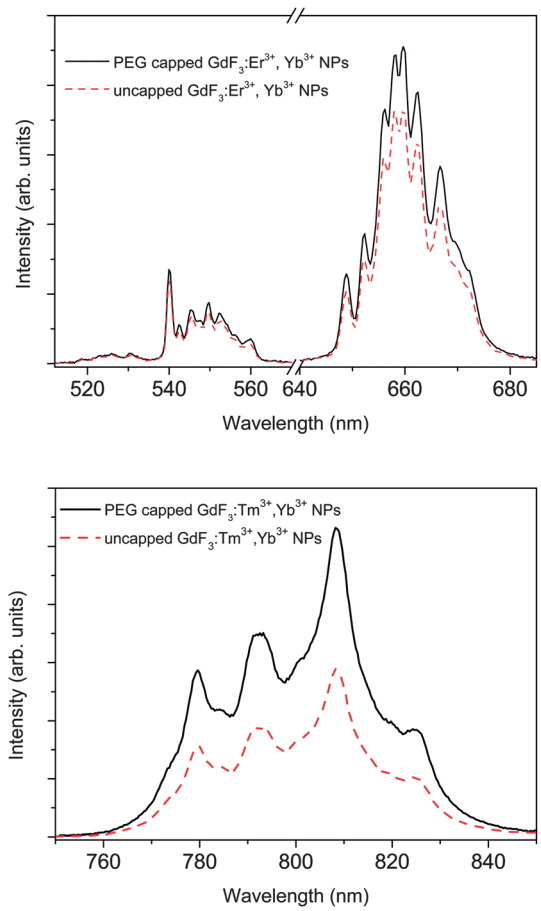

Fig. 4 Comparison between the UC spectra ($\lambda_{exc} = 980$ nm, laser power of 800 mW) of water dispersions of uncapped and PEG-capped Er^{3+}/Yb^{3+} (upper panel) and Tm^{3+}/Yb^{3+} GdF_3 (lower panel) NPs. The spectra have been measured (1.2 g l^{-1} concentration).

the same concentrations (1.2 g l^{-1}) and the same experimental conditions (*e.g.* the pump laser power, signal collection geometry, integration time, slit width of the monochromator). From the obtained spectra, shown in Fig. 4, a significant higher UC emission intensity for the capped GdF_3 NPs than for the uncapped ones can be noted. In fact, an increase of 83% and 25% of the integrated emissions has been observed for the $GdF_3 : Tm^{3+}$, Yb^{3+} and $GdF_3 : Er^{3+}$, Yb^{3+} NPs, respectively. This behavior is a clear indication that the PEG layer on the NP surface reduces the number of water molecules around the lanthanide ions and therefore decreases the emission quenching processes due to the presence of water.

In order to demonstrate the suitability of these materials for NIR-to-red optical imaging, a two-photon confocal image of a water dispersion of the $GdF_3 : Er^{3+}$, Yb^{3+} NPs has been recorded upon exciting laser radiation at a wavelength of 976 nm (Fig. 5) and observing it in the red region (from 620 to 700 nm). The upconversion signal is easily detected with a S/N ratio up to 200, indicating that this material can be successfully used for two-photon optical imaging. Some experiments involving the incorporation of the present NPs into cells are currently in progress.

Before performing any magnetic measurements, the concentrations of the Gd^{3+} ions were determined *via* ICP-MS analysis. Subsequently, measurements of the T_1 (spin-lattice) and T_2 (spin–spin) relaxation times of GdF_3 NPs dispersed in water were performed at 4.7 T. Values of $1/T_2$ *vs.* Gd^{3+} concentration (Fig. 6) were fit using a straight line whose slope determines the transversal relaxivity of the NPs under investigation. Thus, transversal relaxivities of 22.6 ± 3.4 mM^{-1} s^{-1} and 15.8 ± 2.5 mM^{-1} s^{-1} for the Tm^{3+}/Yb^{3+} and Er^{3+}/Yb^{3+} co-doped GdF_3 NPs, respectively, were obtained. On the other hand, substantially lower values, about 0.05 mM^{-1} s^{-1} and 0.02 mM^{-1} s^{-1},

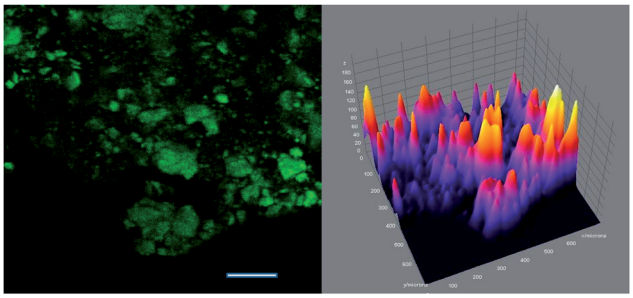

Fig. 5 Coherent Chamaleon Ti-sapphire pulsed laser excited upconversion emission of Er^{3+}/Yb^{3+} doped GdF_3 NPs ($\lambda_{exc} = 975$ nm, pulsed laser power of 330 mW). Scale bar: 100 μm.

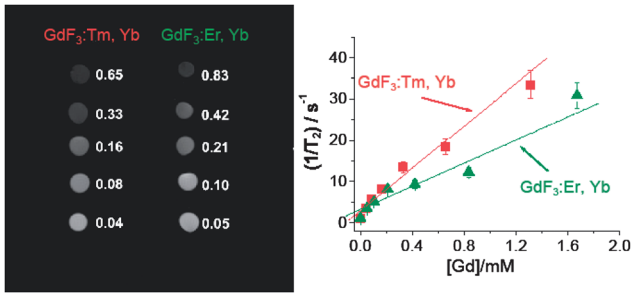

Fig. 6 Left: T_2 weighted (TR = 2000 ms and TE = 75 ms) spin-echo images of water dispersions of PEG-capped GdF_3 NPs for different Gd concentrations (in mM). Right: $1/T_2$ values *vs.* Gd concentration and linear fits (solid lines).

were obtained for the longitudinal relaxivity r_1 for the Tm^{3+}/Yb^{3+} and Er^{3+}/Yb^{3+} co-doped GdF_3 NPs, respectively. Longitudinal and transversal relaxivities were also measured for uncapped Tm^{3+}/Yb^{3+} co-doped GdF_3 NPs and found to be similar (within the experimental error) to the values obtained for PEG-capped NPs.

It is not trivial to compare longitudinal relaxivities of our GdF_3 NPs with values reported in the literature for other compounds, since relaxivities are strongly dependent on experimental conditions such as frequency and temperature. Nevertheless, the r_1 values are lower than those obtained for commonly used MR contrast agents, such as Gd-DTPA[39] (at 1.5 T, r_1 = 4.7 mM^{-1} s^{-1}, r_2 = 5.3 mM^{-1} s^{-1} in water), for Gd^{3+} doped $NaYF_4$ NPs[5] (at 9.4 T, r_1 = 0.14 mM^{-1} s^{-1}, r_2 = 8.7 mM^{-1} s^{-1}) or for PEG-Gd_2O_3 NPs[39] (at 1.5 T, r_1 = 22.8 mM^{-1} s^{-1}, r_2 = 31.2 mM^{-1} s^{-1}, in deionized water). Johnson *et al.*[20] have recently measured the longitudinal relaxivity of ultrasmall $NaGdF_4$ NPs having sizes in the range 8.0–2.5 nm. Longitudinal relaxivities (measured at 60 MHz) ranged between 3 and 7.2 mM^{-1} s^{-1} and decreased with increasing NP size. These results were interpreted by assuming that the Gd^{3+} ions on the particle surface were the major contributors to the longitudinal relaxivity similar to the observed dependence of r_1 on the NP size. As a result, a decrease in the surface/volume ratio is expected with increasing particle size (assuming a spherical particle). Qualitatively, the low values obtained for longitudinal relaxivities in the present study are in agreement with the relevant size of the present rod-shaped NPs (on average, with short and long edges around 85 nm and 150 nm, respectively).

On the other hand, the r_2 values are similar to those found for Gd^{3+} doped $NaYF_4$ NPs, but they are about 3–4 times higher than for Gd-DTPA, suggesting a potential use of the present PEG-capped GdF_3 NPs as negative contrast agents for proton MRI purposes, as also demonstrated below. Moreover, it has been reported that the higher the r_2/r_1 ratio the better the efficiency of a negative contrast agent (Kumar Das *et al.*[40] and references therein). In this respect, Tm^{3+} and Er^{3+} NPs behave like very efficient negative contrast agents having r_2/r_1 ratios of the order of 500 and 800, respectively. The reason for the slight difference in the r_2 values for the Tm^{3+} and Er^{3+} NPs is not yet very clear. The ICP-MS analysis reveals that the molar ratios for the lanthanides are 71.6/2.1/26.3 and 71.4/2.2/26.4 for Gd/Er/Yb or Gd/Tm/Yb in the $GdF_3 : Er^{3+},Yb^{3+}$ and $GdF_3 : Tm^{3+},Yb^{3+}$ NP samples, respectively. These results show that the lanthanide

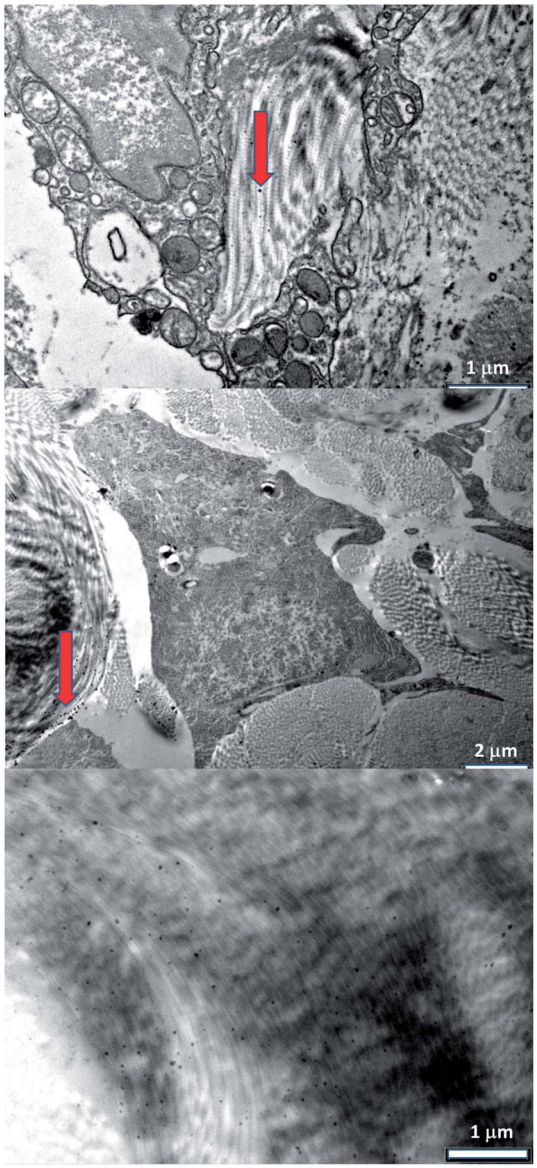

Fig. 7 TEM images of mouse epidermis. Red arrows point to NPs located near collagen fibers.

concentrations are very similar in the two samples, and therefore the small difference in the r_2 values does not originate from different rare earth contents. It is also worth noting that some MRI investigations are reported in the literature considering Er^{3+} and Tm^{3+} complexes[41] but only the T_1-relaxation was studied.

To determine the viability of potentially using these nanomaterials as biological contrast agents, we investigated the cell toxicity of the Er^{3+}/Yb^{3+} or Tm^{3+}/Yb^{3+} co-doped PEG-capped GdF_3 NPs after incubation with adipose mesenchymal stem cells. After six hours of incubation, the percentage of living cells amounted to 65 ± 10% and 58 ± 8%, respectively. After incubation with the commercially available contrast medium Magnevist, 77 ± 6% of the cells were alive. The present results demonstrated that the present GdF_3 NPs were characterized by a relatively low toxic effect on stem cell cultures. To show their *in vivo* viability, the GdF_3 NPs were also injected subcutaneously

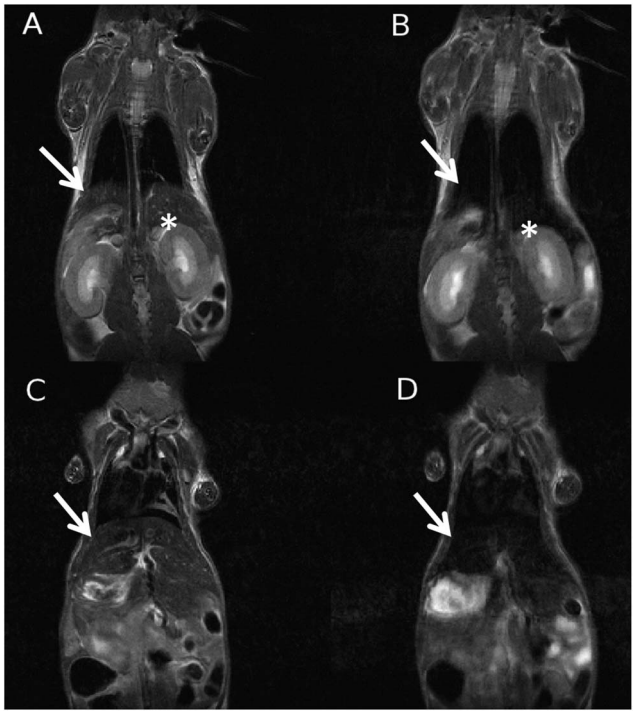

Fig. 8 Coronal MRI slices of a representative animal acquired using RARE T_2-weighted sequences. Mouse images were acquired before (A and C) and 40 minutes after (B and D) the intravenous injection of the GdF_3 NPs. The slice reported in (C) clearly shows the liver of the animal where a loss of the signal of about 45% occurred after NP injection, and (D) indicates the bioaccumulation of the doped GdF_3 NPs in this organ. The slice reported in the upper line clearly shows the kidneys (*) where no appreciable loss of signal was detected.

into a Balb/c mouse, which had no visible acute toxic effects such as a cutaneous rash or oedema 30 minutes after injection of the NPs. TEM analysis performed to evaluate the distribution of the NPs in the dermal compartments showed that the NPs of 80–120 nm were homogeneously distributed in the tissue (see Fig. 7) and specifically NPs were observed in the vicinity of the collagen fiber.

Considering the high values of the r_2/r_1 ratios determined in water, the efficacy of the GdF_3 NPs as negative contrast agents was initially evaluated in mice. Fig. 8 shows MR images (two coronal slices) of a representative animal acquired using a RARE T_2-weighted sequence before (A and C) and 40 min after (B and D) the injection of the GdF_3 NPs. A dosage of 6 mg Gd per kg of mouse was administered. Fig. 8 shows that the liver signal decreased, by about 45%, after NP injection (see arrows). The kidneys are clearly visible in the images reported in the upper line of the figure (asterisks) and no appreciable loss of signal could be detected, up to 40 minutes post-injection.

4. Conclusion

In this article, a facile method for the synthesis of water dispersible Ln^{3+}-doped upconverting GdF_3 NPs is reported. The layer of PEG coating of the GdF_3 NPs ensures a good dispersion of the system in water and reduces the radiationless de-excitation of the excited states of the Er^{3+} and Tm^{3+} ions by water molecules. Strong UC emissions at 650 nm and 800 nm of Er^{3+} and Tm^{3+} ions, respectively, for the codoped GdF_3 NPs, are easily visible by the naked eye. The r_2 relaxivity values (and r_2/r_1 ratios) are quite high, such that the present NPs can be considered as T_2 weighted contrast agents for proton MRI purposes.[24,42,43] Preliminary experiments conducted *in vitro*, in stem cell cultures, and *in vivo*, after subcutaneous injection of the GdF_3 NPs, indicate scarce toxic effects. Up to 40 min after intravenous injection, the GdF_3 NPs localize mainly in the liver as demonstrated by the observed substantial decrease of the MRI signal in this organ. Further experiments in cell cultures and *in vivo* are needed to better investigate the safety profile and usefulness of these NPs in biomedical applications. Nevertheless the present results indicate that NPs are suitable candidates to be efficiently used as bimodal probes for both *in vitro* and *in vivo* optical and magnetic resonance imaging.

Acknowledgements

The authors acknowledge Erica Viviani (Università di Verona, Italy) for expert technical support. This work was supported by Fondazione Cariverona (Verona, Italy), project Verona Nanomedicine Initiative. FV acknowledges the Natural Sciences and Engineering Council (NSERC) of Canada for financial support.

References

1 J. C. G. Bunzli, *Acc. Chem. Res.*, 2006, **39**, 53–61.
2 P. Voisin, E. J. Ribot, S. Miraux, A. K. Bouzier-Sore, J. F. Lahitte, V. Bouchaud, S. Mornet, E. Thiaudière, J. M. Franconi and L. Raison, *Bioconjugate Chem.*, 2007, **18**, 1053–1063.
3 M. D'Onofrio, E. Gianolio, A. Ceccon, F. Arena, S. Zanzoni, D. Fushman, S. Aime, H. Molinari and M. Assfalg, *Chem.–Eur. J.*, 2012, **18**(32), 9919–9928.
4 F. Vetrone, R. Naccache, A. Juarranz de la Fuente, F. Sanz-Rodriguez, A. Blazquez-Castro, E. Martin Rodriguez, D. Jaque, J. Garcia Sole and J. A. Capobianco, *Nanoscale*, 2010, **2**, 495–498.
5 R. Kumar, M. Nyk, T. Y. Ohulchanskyy, C. A. Flask and P. N. Prasad, *Adv. Funct. Mater.*, 2009, **19**, 853–859.
6 J. C. Zhou, Z. L. Yang, W. Dong, R. J. Tang, L. D. Sun and C. H. Yan, *Biomaterials*, 2011, **32**, 9059–9067.
7 F. Vetrone and J. A. Capobianco, *Int. J. Nanotechnol.*, 2008, **5**, 1306–1339.
8 M. Pedroni, F. Piccinelli, T. Passuello, M. Giarola, G. Mariotto, S. Polizzi, M. Bettinelli and A. Speghini, *Nanoscale*, 2011, **3**, 1456.
9 N. N. Dong, M. Pedroni, F. Piccinelli, G. Conti, A. Sbarbati, J. E. Ramírez-Hernández, L. M. Maestro, M. C. Iglesias-de la Cruz, F. Sanz-Rodriguez, A. Juarranz, F. Chen, F. Vetrone, J. A. Capobianco, J. G. Sole, M. Bettinelli, D. Jaque and A. Speghini, *ACS Nano*, 2011, **5**, 8665–8671.
10 M. Botta and L. Tei, *Eur. J. Inorg. Chem.*, 2012, **2012**, 1945–1960.
11 T. Lammers, S. Aime, W. E. Hennink, G. Storm and F. Kiessling, *Acc. Chem. Res.*, 2011, **44**, 1029–1038.
12 A. Accardo, D. Tesauro, L. Aloj, C. Pedone and G. Morelli, *Coord. Chem. Rev.*, 2009, **253**, 2193–2213.
13 G. K. Das, B. C. Heng, S.-C. Ng, T. White, J. S. C. Loo, L. D'Silva, P. Padmanabhan, K. K. Bhakoo, S. T. Selvan and T. T. Y. Tan, *Langmuir*, 2010, **26**, 8959–8965.
14 L. Faucher, A.-A. Guay-Bégin, J. Lagueux, M.-F. Côté, É. Petitclerc and M.-A. Fortin, *Contrast Media Mol. Imaging*, 2011, **6**, 209–218.
15 J. Y. Park, M. J. Baek, E. S. Choi, S. Woo, J. H. Kim, T. J. Kim, J. C. Jung, K. S. Chae, Y. Chang and G. H. Lee, *ACS Nano*, 2009, **3**, 3663–3669.
16 F. Evanics, P. R. Diamente, F. C. J. M. van Veggel, G. J. Stanisz and R. S. Prosser, *Chem. Mater.*, 2006, **18**, 2499–2505.
17 P. Sanchez, E. Valero, N. Galvez, J. M. Dominguez-Vera, M. Marinone, G. Poletti, M. Corti and A. Lascialfari, *Dalton Trans.*, 2009, 800–804.

18 W. Yin, L. Zhao, L. Zhou, Z. Gu, X. Liu, G. Tian, S. Jin, L. Yan, W. Ren, G. Xing and Y. Zhao, *Chem.–Eur. J.*, 2012, **18**(30), 9239–9245.
19 J. Ryu, H.-Y. Park, K. Kim, H. Kim, J. H. Yoo, M. Kang, K. Im, R. Grailhe and R. Song, *J. Phys. Chem. C*, 2010, **114**, 21077–21082.
20 N. J. J. Johnson, W. Oakden, G. J. Stanisz, R. Scott Prosser and F. C. J. M. van Veggel, *Chem. Mater.*, 2011, **23**, 3714–3722.
21 Q. Ju, Y. Liu, D. Tu, H. Zhu, R. Li and X. Chen, *Chem.–Eur. J.*, 2011, **17**, 8549–8554.
22 H.-T. Wong, H. L. W. Chan and J. Hao, *Opt. Express*, 2010, **18**, 6123–6130.
23 W. Qin, C. Cao, L. Wang, J. Zhang, D. Zhang, K. Zheng, Y. Wang, G. Wei, G. Wang, P. Zhu and R. Kim, *Opt. Lett.*, 2008, **33**, 2167–2169.
24 H. B. Na, I. C. Song and T. Hyeon, *Adv. Mater.*, 2009, **21**, 2133–2148.
25 E. Pöselt, H. Kloust, U. Tromsdorf, M. Janschel, C. Hahn, C. Maßlo and H. Weller, *ACS Nano*, 2012, **6**(2), 1619–1624.
26 K. Kaaki, K. Hervé-Aubert, M. Chiper, A. Shkilnyy, M. Soucé, R. Benoit, A. Paillard, P. Dubois, M.-L. Saboungi and I. Chourpa, *Langmuir*, 2012, **28**, 1496–1505.
27 N. Lee, Y. Choi, Y. Lee, M. Park, W. K. Moon, S. H. Choi and T. Hyeon, *Nano Lett.*, 2012, **12**, 3127–3131.
28 C. Sun, K. Du, C. Fang, N. Bhattarai, O. Veiseh, F. Kievit, Z. Stephen, D. Lee, R. G. Ellenbogen, B. Ratner and M. Zhang, *ACS Nano*, 2010, **4**, 2402–2410.
29 H. Lu, L. Guo, N. Kawazoe, T. Tateishi and G. Chen, *J. Biomater. Sci., Polym. Ed.*, 2009, **20**, 577–589.
30 K. Y. Choi, K. H. Min, H. Y. Yoon, K. Kim, J. H. Park, I. C. Kwon, K. Choi and S. Y. Jeong, *Biomaterials*, 2011, **32**, 1880–1889.
31 K. Y. Choi, E. J. Jeon, H. Y. Yoon, B. S. Lee, J. H. Na, K. H. Min, S. Y. Kim, S.-J. Myung, S. Lee, X. Chen, I. C. Kwon, K. Choi, S. Y. Jeong, K. Kim and J. H. Park, *Biomaterials*, 2012, **33**, 6186–6193.
32 L. Lutterotti and S. Gialanella, *ActaMater.*, 1998, **46**, 101–110.
33 A. Masotti, A. Pitta, G. Ortaggi, M. Corti, C. Innocenti, A. Lascialfari, M. Marinone, P. Marzola, A. Daducci, A. Sbarbati, E. Micotti, F. Orsini, G. Poletti and C. Sangregorio, *Magn. Reson. Mater. Phys., Biol. Med.*, 2009, **22**, 77–87.
34 R. Deichmann and A. Haase, *J. Magn. Reson.*, 1992, **96**, 608–612.
35 A. Mukhopadhyay, N. Joshi, K. Chattopadhyay and G. De, *ACS Appl. Mater. Interfaces*, 2012, **4**, 142–149.
36 Y. Zhang, N. Kohler and M. Zhang, *Biomaterials*, 2002, **23**, 1553–1561.
37 C. Yue-Jian, T. juan, X. Fei, Z. Jia-Bi, G. Ning, Z. Yi-Hua, D. Ye and G. Liang, *Drug Dev. Ind. Pharm.*, 2010, **36**, 1235–1244.
38 F. Vetrone, J. C. Boyer, J. A. Capobianco, A. Speghini and M. Bettinelli, *J. Appl. Phys.*, 2004, **96**, 661–667.
39 M. Engstrom, A. Klasson, H. Pedersen, C. Vahlberg, P.-O. Kall and K. Uvdal, *Magn. Reson. Mater. Phys., Biol. Med.*, 2006, **19**, 180–186.
40 G. K. Das, N. J. J. Johnson, J. Cramen, B. Blasiak, P. Latta, B. Tomanek and F. C. J. M. van Veggel, *J. Phys. Chem. Lett.*, 2012, **3**, 524–529.
41 D. Burdinski, J. A. Pikkemaat, J. Lub, P. de Peinder, L. Nieto Garrido and T. Weyhermüller, *Inorg. Chem.*, 2009, **48**, 6692–6712.
42 L. Calucci, G. Ciofani, D. De Marchi, C. Forte, A. Menciassi, L. Menichetti and V. Positano, *J. Phys. Chem. Lett.*, 2010, **1**, 2561–2565.
43 S. Tong, S. J. Hou, Z. L. Zheng, J. Zhou and G. Bao, *Nano Lett.*, 2010, **10**, 4607–4613.
44 R. D. Shannon and C. T. Prewitt, *Acta Crystallogr., Sect. B: Struct. Crystallogr. Cryst. Chem.*, 1970, **26**, 1046–1048.